Classical modeling of positronium cooling in silicon nanochannel plates

Francesco Guatieri,[1,2,3] Sebastiano Mariazzi,[1,2] Christoph Hugenschmidt,[3] and Roberto S. Brusa[1,2]
[1]*Department of Physics, University of Trento via Sommarive 14, 38123 Povo, Trento, Italy*
[2]*TIFPA/INFN, via Sommarive 14, 38123 Povo, Trento, Italy*
[3]*Heinz Maier-Leibnitz Zentrum (MLZ), Technische Universität München, Lichtenbergstr. 1, 85748 Garching, Germany*

(Received 21 February 2022; accepted 11 July 2022; published 21 July 2022)

Silicon nanochannel plates (NCPs) are employed in a variety of experiments as sources of cold positronium (Ps) via positron to Ps conversion. Despite the widespread use of NCPs, no comprehensive model of the dynamics of the cooling process of Ps within the nanochannels has been provided yet. In this work, we present a classical Monte Carlo model of Ps cooling produced in NCPs and validate it against experimental values present in the literature. Our model allows us to estimate crucial characteristics such as the cooling time in NCPs, the angular distribution of emitted Ps, and the fraction of Ps annihilating into three gamma quanta. The simulated energy spectra of emitted Ps closely match experimental results for NCPs held at room temperature. At cryogenic temperature the classical thermalization model does not accurately reproduce the measured spectra, which we attribute to a transition in the cooling process towards a regime where quantum effects play a significant role.

DOI: 10.1103/PhysRevB.106.035418

I. INTRODUCTION

Positronium (Ps) is a purely leptonic atom composed of an electron and its antiparticle, the positron (e^+). Ps exists in two ground states: a triplet state ortho-Ps (o-Ps, vacuum lifetime $\tau = 142$ ns) and para-Ps (p-Ps, $\tau = 125$ ps) predominantly self-annihilating via 3γ or 2γ, respectively. In the last decades, Ps has proved to be a powerful probe for the investigation of porous materials [1–3]. It has been used to characterize the porosities of low-k dielectrics for microelectronics [4–6], gas storage cells and thin membranes for energy applications [7,8], gas sieves [9–11], and drug delivery vehicles [12]. Moreover, Ps is the subject of several fundamental experiments such as spectroscopy of Ps atoms [13–20], the production of antihydrogen by charge exchange [21], probing of gravitational pull on excited Ps atoms [22–24], and the production of Bose-Einstein condensates of Ps atoms [25–28]. All these employ an abundant source of cold positronium. In recent years, efficient sources have been obtained by implanting positrons with an energy of a few keV into silica-based nanostructured films. Both silica-based disordered porous systems [14,29,30] and silicon nanochannel plates (NCPs) [31,32] have been synthesized and employed as efficient Ps sources. In such samples, Ps formation occurs both in the bulk and on the surface of the nanochannels or nanopores [36]. Thanks to this double formation channel and to the high surface-area-to-volume ratio of these samples, a large fraction of implanted positrons can be emitted into the cavities as Ps and by diffusing along interconnected nanochannels or nanopores can eventually be emitted into the vacuum [29,33,34]

Silicon NCPs [35] are silicon single crystals that have been electrochemically etched to create a forest of channels extending from the surface up to a depth of 1 to 2 μm with diameters tuned between 5 and 20 nm. NCP converters exploit a thin layer of silicon oxide (SiO_2) grown on the surface of the channels as an efficient positron to positronium converter [36]. The channel structure forces the Ps atoms (specifically the long-lived o-Ps) to bounce against the walls of the nanochannels several times before they are emitted from the converter. During the transport inside the nanoscopic channels, Ps atoms transfer most of their production kinetic energy of 1–3 eV [36] to the silicon, resulting in a fraction of them to be emitted after having cooled [31,32,37]. Part of this cooled fraction can reach the sample temperature [32].

Measurements of Ps formation and time of flight (ToF) have shown that NCPs are capable of emitting up to 50% of the implanted positrons as positronium [31]. These experiments also provided a measurement of the dependency of the ratio of the 3γ self-annihilation rate and the 2γ Ps-wall annihilation rate as a function of the implantation energy of positrons in NCPs. Characteristic NCP positronium energy spectra display an energy distribution shaped like the convex combination of two thermal distributions: one having temperature close to the sample temperature, the other about one order of magnitude larger [32,38], a phenomenon that as of today still lacks an explanation. Finally, the measurement of the Ps emission angle from NCPs [39,40] has shown a roughly isotropic emission in a 120° cone normal to the NCP surface.

Although qualitative descriptions of the process leading to the production and cooling of Ps atoms in the nanoscopic channels have been presented earlier [31], a quantitative simulation of the process has never been provided. Such a simulation is of high interest as it could be used to adjust the etching process of NCPs to optimize them towards the production of Ps with specific temperature or angular distribution characteristics. Moreover, a quantitative simulation of the mechanisms underlying the NCP positron to Ps conversion would aid the interpretation of experimental data, e.g., by

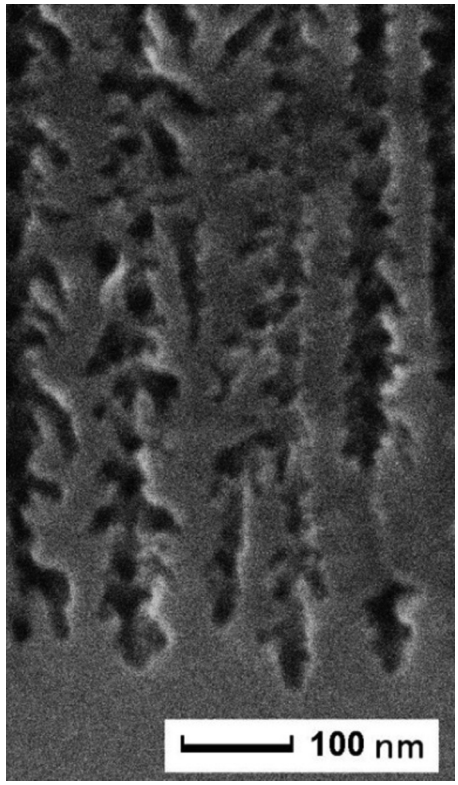

FIG. 1. The SEM imaging of an NCP sample section shows the dendritic structure of the channels, with secondary voids sprouting from the main channel shafts. The sample shown here features larger channels than those employed in the measurements described in the paper; unfortunately it was not possible to SEM image the samples employed in the measurement due to the brittleness of the thinner channels causing them to collapse when the sample is split to be imaged.

providing a solid foundation for Monte Carlo (MC) simulation of experiments employing NCPs.

Any model aimed at delivering a complete description of the cooling process should take into account the fact that, as the energy of the positronium decreases, its wavelength eventually becomes comparable to the channel diameter. A phenomenon of quantum confinement, which would eventually result in a minimum energy that Ps could be cooled to, is expected to take place [41] and, in the case of Ps confined in small pores has been observed [14,42,43]. In perfectly straight channels the effects of quantum confinement are expected to only affect Ps momenta in the direction orthogonal to the surface [41], nonetheless due to the corrugation and irregularity of the channels in our samples (see, e.g., Fig. 1), it is reasonable to assume that such effects would manifest in all components of the emitted Ps momentum. This assumption is corroborated by recent experimental observations [44]. We therefore do not expect a completely classical model to be able to properly describe the cooling process in extremely thin channels or in cryogenically cooled NCPs; nonetheless, we will show that for larger channels and higher temperatures such a model can be produced.

In this work we present a quantitative classical model capable of describing effectively the cooling process of Ps in NCPs. In Sec. II, we formulate a classical model of Ps cooling in NCP. Such a model is based on a geometrical description of the NCP structure previously employed to simulate positron implantation and the subsequent diffusion in order to determine the depth distribution of the produced Ps [35]. In Sec. III we calibrate the classical model on results reported in literature and then apply it to simulate the energy spectra of Ps emission from NCP and to gain some insight over the origin of the two-thermal-distribution-shaped spectra whose observation is present in the literature [32,38] but never explained. Finally, we use this classical model to fit recent measurements [45] showing that the model can predict the Ps spectrum emitted by room-temperature NCPs using realistic parameters, but not that of cryogenically cooled ones. Given the previous literature on the topic [14,41,42] we ascribe this phenomenon to a transition from the classically described cooling to quantum effects that manifest in presence of smaller channels or colder samples.

II. FORMULATION OF THE MODEL

The problem of simulating the implantation profile for positrons in a NCP converter and its diffusion towards the surface of a channel has been discussed in detail in [35], in which implantation and production profiles for samples with the same channel length as those employed in this work are reported. Based upon that result we have developed a completely classical model of the cooling and transport of Ps within the nanoscopic channels. This simulation can also provide the angular distribution of the emitted Ps atoms and their permanence time in the nanoscopic channels (see Sec. II C and Appendix A). In [35] the geometric model of an NCP converter channel was developed as the union of the volumes of truncated cones and spheres, a geometric shape there named *dendrite*. The converter geometry was then obtained by subtracting numerous *dendrites* from the volume of a half-space. The Ps cooling in the full NCP geometry is studied and, when relevant, the results obtained by running the simulations within a single dendrite or a cylindrical channel will be shown too. These comparisons are of interest since simulations employing the NCP geometry are computationally demanding; therefore, wherever the use of single dendrites or cylindrical channels yields similar results, the replacement of the full geometry can significantly speed up the computation [46]. Unless otherwise specified, when employing single dendrites, we will be generating them with the same parameters employed for the entire NCP structure.

The energy spectrum of positronium produced in SiO_2 manifests two main emission energy peaks located at 1 and 3 eV attributed, respectively, to Ps production in the bulk and to Ps produced at the surface [36,47]. Since the SiO_2 layer of our NCPs has a thickness in the order of nanometers [31] we can assume a δ distribution centered at 3 eV as a suitable model for the production energy spectrum of Ps inside of the sample channels.

We will model the interactions between the positronium and the channel walls as a series of discrete interactions. The validity of this approach may become disputable at the end of the thermalization process as the de Broglie wavelength of a thermal Ps atom becomes comparable to the radius of

the nanoscopic channel [37,41]. The scattering process of a Ps atom against a nanochannel wall is modeled using a single interaction process. Since as of today no experimental data are available inquiring directly the scattering interaction between a Ps atom and a surface coated in SiO_2, we started by testing the simplest reasonable model. As a first attempt, we will assume completely isotropic scattering angles, i.e., the outgoing positronium angle is assumed to be uniformly distributed in the 2π solid angle allowed by the surface geometry (for uniformity with the parametrization that will be introduced in Sec. III C this scattering model will be referred as $q = 1$ model in plot captions and labels). This choice is motivated by the fact that scanning electron microscopy (SEM) of NCPs (see Fig. 1) showed extremely irregular surfaces that can degenerate, in some cases, in additional cavities connected to the main channel shaft.

We will model the energy loss due to a scattering with the wall by first drawing a random particle from a thermalized ideal gas, then simulating an elastic scattering between the impinging Ps and such particle and then taking the final Ps energy as its energy after it hits the wall. This model corresponds to the one proposed by Sauder [48] to describe Ps thermalization in rare gases which has been widely and effectively used [49–52]. In his model Sauder assumed isotropic elastic scattering between Ps and atoms of the gaseous moderator, then computed the average energy loss after each interaction. Since we do not aim to compute merely the average energy after n interactions but, instead, the complete energy probability distribution after n interactions, we need to expand Sauder's model and employ the entire energy-loss distribution (not only its mean) to evolve the Ps energy spectrum.

Under these premises we can split the simulation process into three phases:

(i) Computing the energy spectrum $\mathcal{K}_n(E_{Ps})$ of a distribution of Ps atoms generated at 3 eV and each having undergone exactly n interactions (see Sec. II A).

(ii) Computing the probability $F_S(n)$ that a Ps in a capped channel will survive n interactions without annihilating (see Sec. II B).

(iii) Computing the *interaction count spectrum* $\mathcal{S}(n)$, defined as the probability that an infinitely lived Ps generated within a channel will interact exactly n times before escaping into the vacuum (see Sec. II C).

After all three components have been computed we can write the energy distribution $\mathcal{K}(E_{Ps})$ of the emitted positronium as

$$\mathcal{K}(E_{Ps}) = \frac{1}{k}\sum_{n=0}^{\infty}\mathcal{S}(n)\mathcal{K}_n(E_{Ps})F_S(n) \tag{1}$$

with the normalization

$$k = \sum_{n=0}^{\infty}\mathcal{S}(n)F_S(n). \tag{2}$$

The summations to ∞ can be cut to a finite value of n that still provides a good estimation of the limit value since both $\mathcal{S}(n)$ and $F_S(n)$ asymptotically tend to zero as an exponential law or better.

On top of allowing the computation of the energy spectrum $\mathcal{K}(E_{Ps})$, these three components allow the computation of the fraction $f_{3\gamma}$ of the implanted positrons annihilating into three gamma quantas and the Ps emission angle from the NCP. We will show later on how these quantities can be computed enabling us to tune and validate our model. In Appendix A we will show how the Ps average permanence time in the NCP channels can be computed using our model.

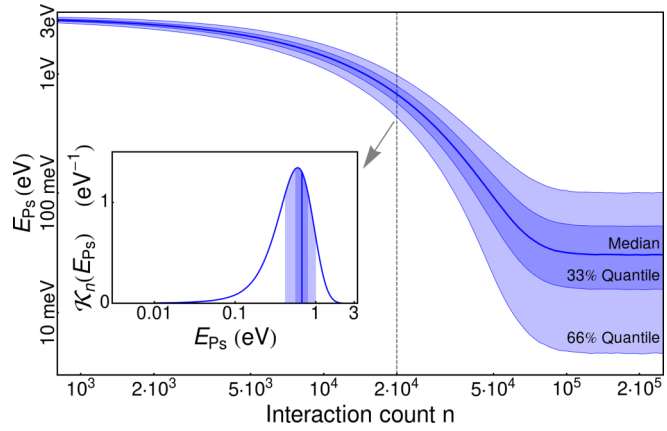

FIG. 2. MC simulation of the evolution of a δ distribution of Ps (centered at 3 eV) having each undergone n elastic scatterings in a gas of particles with a temperature of 300 K and a mass of 28 u. To each position of the x axis corresponds an energy distribution. The distributions in the central region ($n \approx 10^{3.5\text{–}4.5}$) are bell shaped (see inset) and converge to a Maxwell-Boltzmann distribution for $n \to \infty$.

A. Thermalization dynamics of Ps

To describe the energy-loss process, a Ps atom is assumed to be traveling with speed $\vec{v}_i$ before it interacts elastically with an atom of mass M traveling at speed $\vec{v}$. Imposing the conservation of momentum an energy does not determine the final Ps speed $\vec{v}_f$ but forces it to lay in the locus:

$$\begin{aligned} \vec{v}_f &= \vec{w} + \hat{u}\cdot r \\ \text{with}\quad \vec{w} &= \vec{v}_i\cdot\frac{m}{m+M} + \vec{v}\cdot\frac{M}{m+M} \\ \text{and}\quad r &= |\,\vec{w}-\vec{v}_i\,|, \end{aligned} \tag{3}$$

where m is the Ps mass and $\hat{u}$ is a random vector of length one. The scattering can be simulated in one, two, or three spatial dimensions (see Secs. 16 and 17 of [53]). If $\hat{u}$ is uniformly drawn, as required by the isotropic scattering model [48], then an arbitrary velocity distribution of Ps will converge after a suitable number of wall interactions to a thermal distribution with a dynamic that is independent on the dimensionality in which the problem has been solved (that is regardless of $\hat{u}$ having been picked from the unitary circle, the unitary sphere or the $\{\pm 1\}$ set). The thermalization dynamic with M set to the mass of a silicon atom is shown in Fig. 2.

Due to the lighter element in the sample composition being the oxygen we do not expect the value of the effective mass to be less than 16 u. Previous works that employed Sauder's model to study Ps thermalization with silica powders [50] found values of M ranging up to 112 u; we expect therefore

TABLE I. d_B computed for single dendrites and the NCP geometry detailed in [35]. We report in the last column the ratio between d_B and the mean radius of the channels, which is exactly 2 in the case of cylindrical channels [55].

Geometry	$R_{\min}$	$R_{\max}$	d_B	$\frac{d_B}{\langle R\rangle}$
Cylinder	R	R	$2R$	2
Dendrite	3 nm	4 nm	6.8 nm	1.94
Dendrite	4 nm	6 nm	9.7 nm	1.94
Dendrite	5 nm	8 nm	12.8 nm	1.94
Dendrite	7 nm	9 nm	15.6 nm	1.95
NCP	3 nm	4 nm	8.6 nm	2.46
NCP	4 nm	6 nm	15.0 nm	3.00
NCP	5 nm	8 nm	25.5 nm	3.92
NCP	7 nm	9 nm	43.6 nm	5.45

realistic values for M to be comprised in the $16\,\mathrm{u} < M < 112\,\mathrm{u}$ range.

B. Ps annihilation within the channels

Ps annihilation inside of the nanoscopic channels can be independently caused by two different processes: the Ps self-annihilation into 3γ with a lifetime of 142 ns and 2γ annihilations caused by the interaction with the channel walls. Similarly to [54] we will impose that every time a Ps scatters against the wall of a channel it will have a fixed probability p of annihilating into two gamma quanta.

In order to determine the self-annihilation probability as a function of the interaction count we need to employ the Ps speed and the average distance d_B between successive interactions. In the case of a cylindrical channel of radius R, this quantity is exactly $d_B = 2R$ [55]; and this value works fairly well as an approximation of d_B in a single dendritic channel. The distance of the $d_B/\langle R\rangle$ from the value 2 is a measure of how much single dendrites can predict the $2\gamma/3\gamma$ annihilation ratio. Values above 2 indicate geometries with lower $2\gamma/3\gamma$ annihilation ratio, i.e., higher 3γ self-annihilation rate, than predicted by single dendrites. To simulate cooling in NCPs, d_B can be computed via MC simulation as summarized in Table I. Using an entire NCP has the effect of increasing the value of d_B, due to the channels occasionally merging together. Varying the channel radii $R_{\min}$ and $R_{\max}$ while maintaining constant their density per unit of macroscopic surface shows that larger channels merge more frequently, leading to further departure from the single dendrite case.

By employing d_B and the speed distribution of Ps after n iterations we can compute the average time t_B between successive wall interactions for a Ps atom that already underwent n wall interactions. Taking into account the wall annihilation probability p we can recursively compute the probability $F_S(n)$ that a Ps will survive more than n interactions as

$$\begin{aligned} F_S(0) &= 1, \\ F_S(n+1) &= F_S(n)(1-p)e^{-t_B(n)/\tau}. \end{aligned} \tag{4}$$

Similarly we can compute which fraction will have decayed into two ($F_{2\gamma}$) or three gammas ($F_{3\gamma}$) within the same amount of interactions as

$$\begin{aligned} F_{2\gamma}(0) &= 0, \\ F_{3\gamma}(0) &= 0, \\ F_{2\gamma}(n+1) &= F_{2\gamma}(n) + F_S(n)p, \\ F_{3\gamma}(n+1) &= F_{3\gamma}(n) + F_S(n) \\ &\quad \times (1-p)(1-e^{-t_B(n)/\tau}). \end{aligned} \tag{5}$$

Note that

$$F_S(n) + F_{2\gamma}(n) + F_{3\gamma}(n) = 1 \quad \forall\, n.$$

An example of the evolution of the three populations with the number of wall interactions is given in Fig. 3.

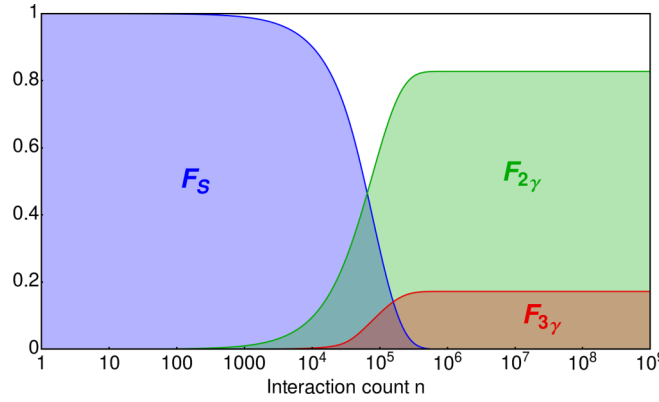

FIG. 3. The surviving fraction of positronium (F_S), the wall-annihilating fraction ($F_{2\gamma}$), and the self-annihilated fraction ($F_{3\gamma}$) as a function of the number of interactions with the channel walls. The simulation has been performed for a 300 K wall, effective channel radius 12 nm, effective mass $M = 16\,\mathrm{u}$, and annihilation probability during a single interaction $p = 10^{-5}$.

Saito and Hyodo [54] provide an estimate for the value of p in the form of the quenching rate λ in a cavity. If we convert these in their equivalent value for p assuming the Ps to be traveling (for consistency with [54]) at 10^5 m/s we obtain $p \approx 10^{-5}$ which we will use as a reference value hereafter for the p parameter.

C. Interaction count spectrum

The probability that an infinitely lived Ps will require exactly n wall interactions to exit the nanoscopic channel $\mathcal{S}(n)$ can be numerically computed through MC simulations. Interaction count profiles for entire NCPs described using the model and the parameters of [35] are shown in Fig. 4. In order to mimic the interaction count spectrum obtained from the NCP geometry we attempted to use single dendrites from the same NCP or cylindrical channels of comparable radius and length. In both cases, however, $\mathcal{S}(n)$ differs greatly from the NCP geometry and its proposed mockups. To search for better performing substitutes of the full NCP geometry, we employed MC simulations to compute, for different NCP construction parameters, an *effective* radius for the NCP channels, i.e., a value chosen such that a cylindrical channel or a single dendrite of this effective radius would give a $\mathcal{S}(n)$ spectrum very close to the one obtained with the full NCP.

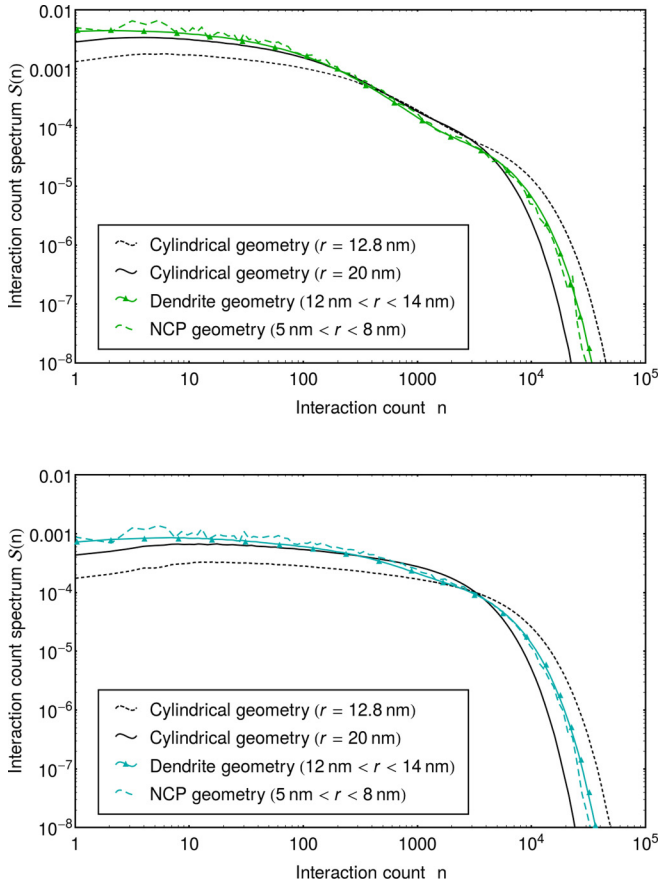

FIG. 4. Interaction count spectrum $\mathcal{S}(n)$ within the NCP geometry (generated with the parameters given in [35]) for a 7-keV (above) and 11-keV positron implantation energy (below). Overlaid in the same color is the spectrum given by single dendrites generated with radii that reproduce the value of d_B observed in the NCP. Black curves correspond to the interaction count spectra of cylindrical channels with radii equal to the NCP effective radius (dotted line) or chosen to reproduce as closely as possible the NCP spectrum (continuous line). The bump shown in the 7-keV spectrum above 1000 hits is due to the finite length of the channels.

The result is that the single dendrite model is capable of closely mimicking an entire NCP with 5–8 nm radius channels, when an effective radius of 12–14 nm is used (see Fig. 4). On the contrary, no effective radius for the cylindrical geometry is able to mimic the full NCP spectrum. The need to increase the effective radii in the dendrite geometry to emulate the behavior of an NCP structure comes from the presence of intersections between NCP channels that the single dendrite cannot account for. As the probability of channel intersecting decreases strongly with the volume occupied by each single dendrite, the discrepancy between actual NCP channel radius and the effective dendrite radius deceases along with the NCP channel radius. With channel radii smaller then 3 nm, the actual and effective radii coincide. These observations can be summarized into the fact that we can employ a single dendrite with the correct effective radius to compute $\mathcal{S}(n)$ resulting in a considerable reduction in computational complexity and time [46].

III. VALIDATING THE MODEL ON EXPERIMENTAL DATA

The fraction of implanted positrons annihilating via three gammas as a function of the positron implantation energy E [$f_{3\gamma}(E)$], the angular distribution of Ps emission into vacuum, and the emitted Ps energy spectra have been measured in the past years [31,32,39,45,57,58]. We validated our model by simulating all the experimental results obtained so far.

A. 3γ fraction

References [32,58] provide a measure of the fraction $f_{3\gamma}(E)$ of the implanted positrons decaying in the target or in its vicinity into three gamma quanta instead of two. We can use our model to try to predict this quantity [55].

We start by computing the fraction of produced Ps that decays into three gammas as

$$S_{3\gamma}^{\mathrm{Ps}}(E) = \sum_{n=0}^{\infty} \mathcal{S}(n)[1 - F_{2\gamma}(n)]. \tag{6}$$

To compute from this the fraction of the implanted positrons that decays into three gammas we need to provide a value for the probability $\epsilon_{\text{o-Ps}}$ that a thermal positron reaching the SiO_2 surface will be reemitted as o-Ps. Mills experimentally determined this parameter [59] as the limit of the o-Ps production efficiency from a silica surface as the implantation energy approaches zero obtaining values of $0.38^{+5\%}_{-10\%}$ and $0.44^{+5\%}_{-10\%}$ for differently aged samples. The measurement by Mariazzi *et al.* [32] provides a value of 0.42 ± 3.5 for $\epsilon_{\text{o-Ps}}$. More recent measurements [60] showed o-Ps production rates up to 70%. Given this range of values, we can in principle expect the exact value of $\epsilon_{\text{o-Ps}}$ to be dependent on the specific NCP sample, but to be comprised in the 40%–70% range. Varying the value of $\epsilon_{\text{o-Ps}}$ has the effect of changing the absolute amount but not the shape of $f_{3\gamma}(E)$.

We can compute $f_{3\gamma}(E)$ as

$$f_{3\gamma}(E) = \frac{\epsilon_{\text{o-Ps}}}{1 - f_{\text{BS}}(E)}\left[S_{3\gamma}^{\mathrm{Ps}} f_N(E) + f_M(E)\right], \tag{7}$$

where $f_{\text{BS}}(E)$, $f_N(E)$, and $f_M(E)$ are, respectively, the fraction of the implanted positrons being backscattered from the sample, the fraction reaching, thermalized, the surface of a channel, and the fraction reaching, thermalized, the surface of the sample. Details on how these quantities are computed can be found in Ref. [35].

The result of such computation is shown (dashed lines) in Fig. 5 alongside the experimental values (black symbols). Experimental results and simulation display a significant discrepancy which cannot be resolved by tuning the parameters M, p and the dendrite geometry within realistic limits. This is the first of two experimental tests that this model is incapable of describing correctly. We will illustrate briefly the other two before showing how the model can be altered to correctly reproduce the experimental data (colored continuous lines in Fig. 5).

B. Angular distribution

A by-product of the MC simulations needed to compute the *interaction count spectrum* $\mathcal{S}(n)$ is the angular distribution of Ps being reemitted into vacuum, as it consists of the

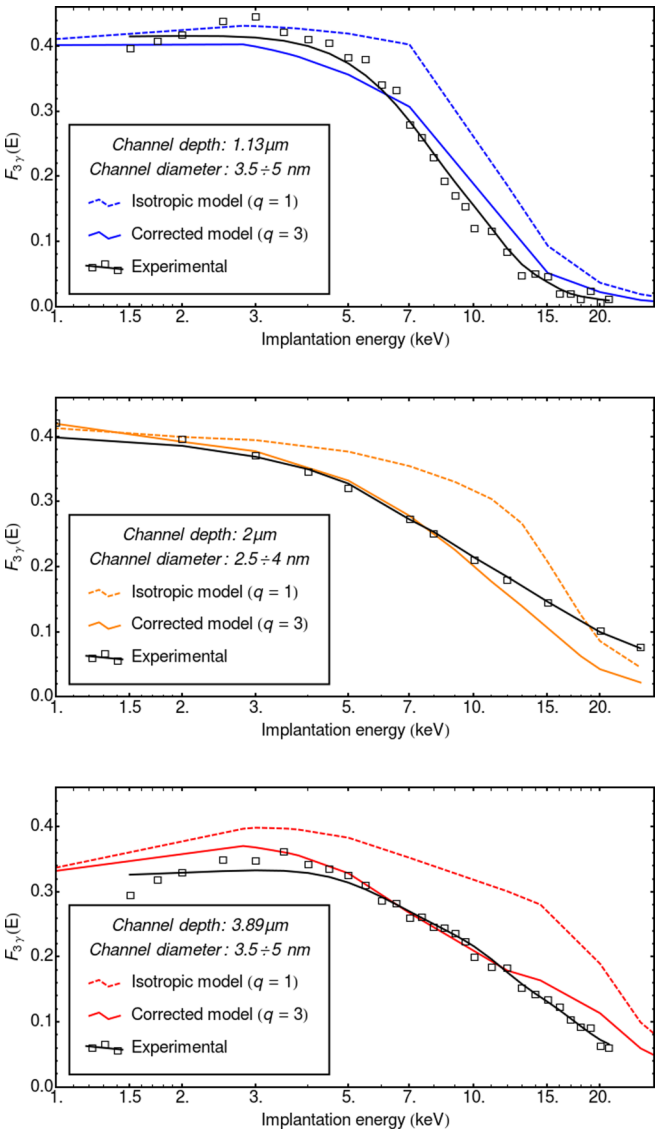

FIG. 5. $f_{3\gamma}(E)$ fraction as predicted by our model for three different NCP samples (dashed line for the isotropic model and continuous colored line for the corrected model) and as measured (symbols and continuous black line). The topmost and lowermost plots show our model being compared with the measurements presented in Ref. [58], the middle one compares to Ref. [32]. The geometry employed for the simulations is single dendrites generated using the effective radius. We can see in all three instances how the corrected model predicts much more accurately the experimental data.

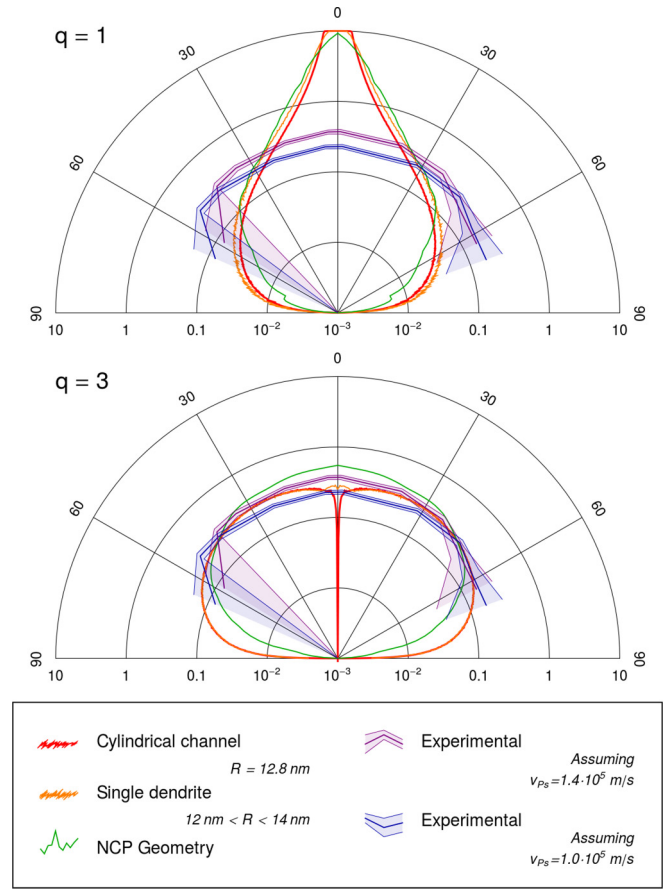

FIG. 6. Ps emission angle measured from the macroscopic surface normal (blue and purple) [39] as well as the distributions computed by employing the isotropic model with $q = 1$ (above) and $q = 3$ (below). The simulations are performed on the full NCP geometry and on simpler geometries with cylindrical channels or single dendrites. Note that the simpler geometries perform similarly. We furthermore observed that the dependency of the result on the channel radius is extremely weak. The spikes visible at $\alpha = 0^\circ$ in the second panel are caused by the asymptote in the normalization.

distribution of the trajectories of the Ps atoms when they have reached the end of the simulation. An experimental value for such quantity has been computed in Ref. [39], by employing data from the AEgIS positron system [61]. In Fig. 6 the emission angle distributions for the three geometries hereupon considered are shown superimposed to the experimental curve in Ref. [39], showing once again a discrepancy between the simulation and the experimental data. By comparing simulations run over different geometries we have observed that the angular distribution given by the full NCP can be loosely approximated by employing single dendrites or cylindrical channels instead.

C. Tuning the model

Up until here the model was found to fail to reproduce the experimental data obtained for $f_{3\gamma}$ and emission angle. If we closely analyze the various discrepancies, we see that they all point towards a single direction: Ps appears to escape the nanoscopic channels after undergoing too few interactions. Among these discrepancies, the angular distribution of the emitted Ps is of particular interest since it depends only on the sample geometry and on the scattering model.

Since this discrepancy could not be fixed within realistic variation of the sample geometry, the assumed uniform Ps scattering angular distribution is obviously not reasonable. Therefore, we now replace this model with a scattering cross section dependent on an empirical parameter q capable of tuning it to be more or less forward directed. A computationally convenient choice is to employ a polar coordinate system

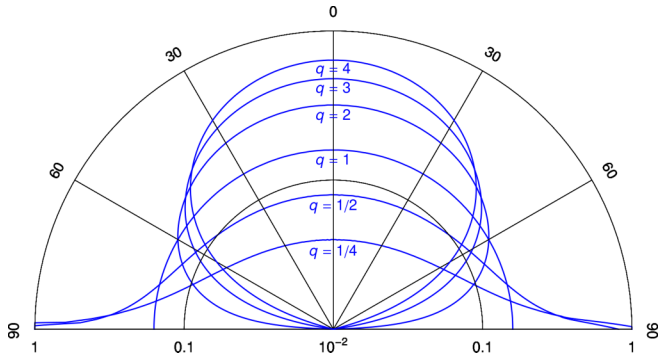

FIG. 7. Angular distribution model for the positronium atoms bouncing off the wall of a nanoscopic channel for different values of q.

centered on the channel wall with axis orthogonal to the channel wall itself; and drawing the polar angle ϕ from a uniform distribution and generate the azimuthal angle θ by computing

$$\theta = \cos^{-1}(\Theta^{1/q}), \tag{8}$$

where Θ is a random variable uniformly distributed in the interval [0,1] and q is the parameter that determines how forwardly distributed the distribution should be. The resulting scattering model is analogous to the scattering model employed by Phong [62], which has proved effective in describing the scattering of optical photons by corrugated surfaces with unknown microscopic structure. For $q = 1$ this distribution is uniform over the 2π solid angle. For $q > 1$ the distribution becomes forward heavy and for $0 < q < 1$ it becomes lateral heavy. In Fig. 7 we show the shape of the distribution for different values of q.

By trying different values of q we found that $q = 3$ fairly reproduces the experimental data on the Ps emission angle distribution (see Fig. 6). The lowermost panel in Fig. 6 shows the revised angular distribution which, in particular when employing the full NCP geometry, presents a much better agreement with the experimental values. It is noteworthy that for all practical purposes values of d_B computed with $q = 3$ are indistinguishable from values of d_B computed with $q = 1$.

A comparison of interaction count spectra computed with $q = 1$ and with $q = 3$ is shown in Fig. 8, displaying how the number of collisions has increased considerably while, at the same time, most features of the spectra are conserved (including the bump due to the reflection on the channel's bottom end). Once again the single dendrite geometry employed with an effective radius is capable of properly mimicking the interaction count spectrum given by the full NCP geometry.

The 3γ fraction given by the Ps scattering angular distribution, shown as the orange curve in Fig. 5, achieves a good agreement with the experimental data up to an implantation energy of 9 keV.

D. Energy spectra

Figure 9 shows an example of the Ps energy spectrum computed using Eq. (1) with $q = 3$. The resulting curve can be fitted surprisingly well with a combination of two thermal distributions, one close to room temperature and the other at

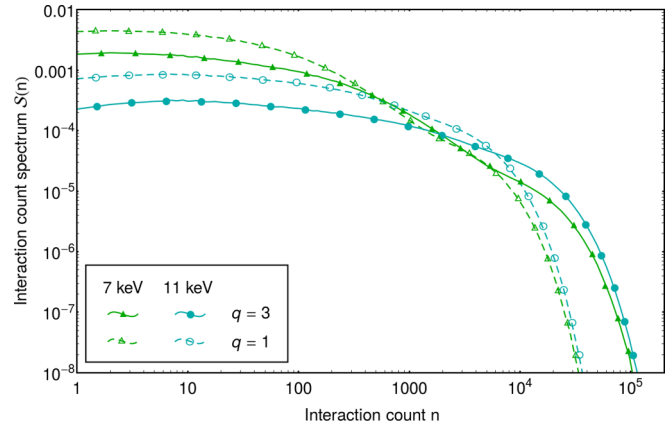

FIG. 8. $\mathcal{S}(n)$ profiles for the single dendrite geometry (12 nm $< R <$ 14 nm) for $q = 1$ (uniform distribution) and $q = 3$ (angular distribution).

a much higher temperature. This is in excellent accordance with the previous literature that repeatedly found the emitted positronium distribution to consist, supposedly, of the sum of two distinct thermal populations [32,38,63]. We will provide a more detailed explanation of the phenomenon in Appendix B; for the scope of this section we will restrict ourselves to characterize phenomenologically this behavior.

We expect the kinetic energy distribution of particles in a thermalized gas to follow the probability distribution

$$\mathcal{D}(E_{Ps}, T) = \frac{2}{\sqrt{\pi}}\left(\frac{1}{k_B T}\right)^{3/2} \sqrt{E_{Ps}}\, e^{-E_{Ps}/(k_B T)} \tag{9}$$

with k_B being the Boltzmann constant, T the temperature of the gas, and E_{Ps} the kinetic energy of the particle. Since in our simulations we consider the totality of the positronium emitted by the NCP we adopt a three-dimensional Maxwell-Boltzmann distribution. We employ Eq. (9) to formulate a proper fit model for the simulated spectra as

$$\mathcal{K}(E_{Ps}) = f\mathcal{D}(E_{Ps}, T_1) + (1 - f)\mathcal{D}(E_{Ps}, T_2). \tag{10}$$

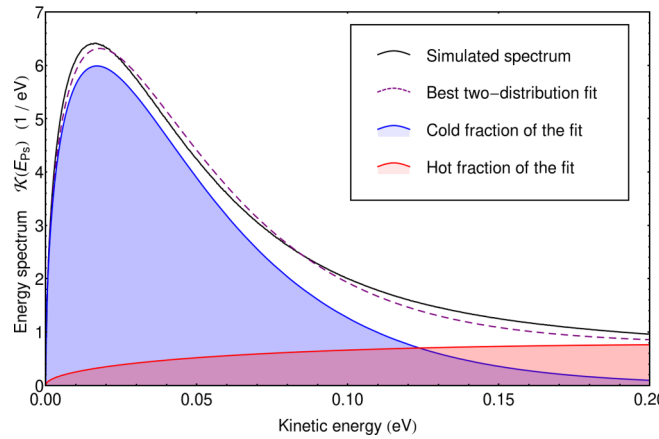

FIG. 9. Simulated Ps kinetic energy spectrum (black line) and the model of Eq. (10) fitted upon the simulated spectrum (dashed purple), with its cold (filled blue) and hot (filled red) components.

TABLE II. Least-squares fit of the effective mass M over experimental data from [45]. The effective mass given by the fit over room-temperature data yields values consistent with oxygen. The fit over cryogenically cooled NCPs gives lower values (see text).

Implantation energy	NCP temperature	M
7 keV	300 K	17.6 ± 2.4 u
7 keV	20 K	0.2 ± 0.4 u
11 keV	20 K	0.5 ± 0.3 u

We fitted the spectra obtained from the simulator employing the model of Eq. (10) with the constraints $0 \leqslant f \leqslant 1$ and $T_1 < T_2$. The result of the fit process for a single spectrum is shown in Fig. 9. For this example, the simulated energy spectrum has been obtained using dendritic channels with $2\,\text{nm} < R < 4\,\text{nm}$, an effective mass of 28 u, a sample temperature of 300 K, $q = 3$, implantation energy 7 keV, and a wall annihilation probability of 10^{-5}. The low value for the effective mass has been chosen to provide an energy distribution closer to full thermalization. From the fit performed using Eq. (10), a fraction of 42% of the simulated Ps atoms belongs to a cold component with a temperature $T_1 = 395\,\text{K}$ and the rest to a hot one with $T_2 = 5650\,\text{K}$.

Reference [45] reports the measurement of the energy spectrum of Ps emitted from NCPs at room and cryogenic temperature. We can apply our model to predict the energy spectrum measured by the experimental setup of [45] as a function of the effective mass M. Due to the finite acceptance volume of the ToF experimental setup and the permanence time effects, we need to include a model of the experimental apparatus itself in the MC simulation to properly predict the shape of the measured spectra, as described in [55]. By running multiple simulations with varying values of M, we can perform a least-χ^2 fit over the experimental data to deduce the effective mass; if the model is capable of predicting the spectra produced by an NCP, we expect the resulting value to be compatible with the chemical composition of the NCP walls. Table II shows the result of the least-χ^2 fit of M over the measurements in [45], and the value of 17.6 u for room temperature NCPs lies in-between the atomic mass of oxygen and that of silicon.

For cryogenically cooled NCP the fit yields very low effective mass values, as we can see from the table. At low temperature, the de Broglie wavelength of Ps is similar to the dimension of the channels and quantum effects become dominant. An effective mass lower than 16 u in the classical model indicates that the Ps is being cooled more efficiently at low temperature than at room temperature in the nanochannels.

A recent paper [43] has analyzed the cooling of Ps in closed pores in silica, showing that, in that case, a dependency of the effective mass on Ps energy needs to be introduced to correctly reproduce the experimental data at low temperature. In that work, the effective mass increases as the Ps energy decreases, indicating that cooling at cryogenic temperatures is less efficient than at room temperature. The different behavior of the effective mass in closed porous silica and in NCPs could be explained by the different geometry of the two systems. Indeed, the energy spectra of Ps trapped inside voids (namely, in small voids [41] but also in large pores with surface states [56]) are discrete. Consequently, at low temperature, when quantum effects become dominant, the cooling process is expected to be slowed down by the reduced availability of energy levels. On the contrary, the energy spectra of Ps trapped inside of channels are predicted to be continuous [41] with no hindering of the cooling in one of the three dimensions. Moreover, due to the larger de Broglie wavelength, Ps can simultaneously probe more scattering centers which can result in a low effective mass in the classical elastic scattering.

IV. CONCLUSIONS

A classical model of the Ps cooling inside the nanochannels has been developed. The model has been validated on previous measurements, performed in samples held at room temperature of the angular distribution of Ps emitted by NCP samples and 3γ annihilation fraction ($f_{3\gamma}$), showing that a purely classical description of the Ps cooling in room-temperature NCP converters is possible. In particular, the model was shown to predict the lower end of the spectrum to be shaped as the sum of two thermal distributions, as was previously observed experimentally. We have shown that the model fails to properly describe energy spectra of Ps emitted by cryogenically cooled NCP converters, which due to quantum confinement is expected.

The proposed classical cooling model could be used to optimize NCP targets in order to deliver large amounts of Ps close to room temperature. In the future, we plan to combine the present classical model with quantum models (see, for example, [41]) to get a full understanding of the cooling process even at temperature in the range of few tens of Kelvin. This would allow the optimization of the design of NCPs for the production of ultracold Ps.

ACKNOWLEDGMENTS

We would like to thank Dr. D. Orsucci whose time, help, and patience greatly contributed to the improvement of this research work.

APPENDIX A: PERMANENCE TIME

The permanence time of a Ps atom in an NCP, defined as the time lapsed between the Ps atom production inside of the converter and the moment at which it is emitted by the NCP converter, can be directly computed in a MC simulation. More conveniently, the mean value of the permanence time can be computed, in the model presented in this paper, as

$$T_P = \frac{\sum_{n=0}^{\infty} \mathcal{S}(n) F_S(n) t_F(n)}{\sum_{n=0}^{\infty} \mathcal{S}(n) F_S(n)}, \tag{A1}$$

where $t_F(n)$ is the average time necessary for a Ps atom to interact n times with the channel walls. It is possible to compute $t_F(n)$ from $t_B(n)$ (see Sec. II B for the definition) as

$$t_F(n) = \sum_{i=0}^{n} t_B(i). \tag{A2}$$

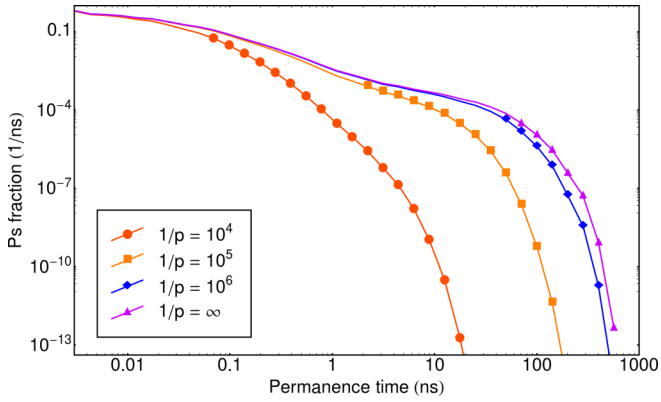

FIG. 10. Distribution of permanence times for Ps atoms emitted by an NCP, as predicted by our model. The positrons are implanted with an energy of 7 keV, scattering parameter $q = 3$, and every other parameter identical to those employed to compile Table III.

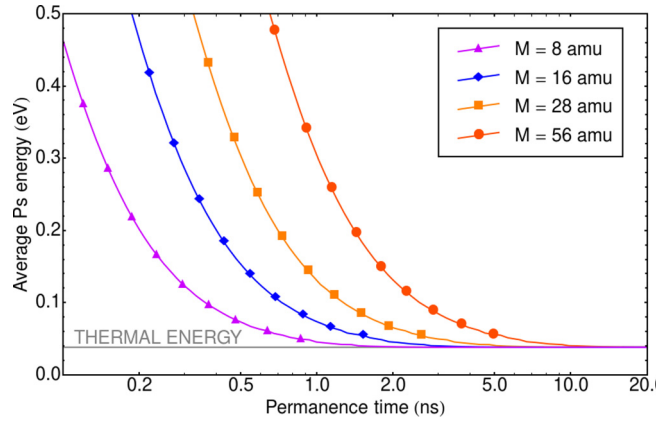

FIG. 11. Dependency of the average Ps atom energy as a function of their permanence time, as predicted by our model. The positrons are implanted with an energy of 7 keV in a sample held at 300 K, scattering parameter $q = 3$, wall annihilation probability $1/p = 10^5$, effective mass M as indicated in the plot, and every other parameter identical to those employed to compile Table III.

The permanence time is unique to each emitted Ps atom, and its value is highly correlated with the Ps atom kinetic energy. Figure 10 shows the distribution of permanence times in Ps atoms emitted from an NCP as predicted by our model; the shape of the distribution is similar to that of the interaction count spectrum $\mathcal{S}(n)$, albeit not identical as it is distorted by both the nonlinear nature of $t_F(n)$ and the exponential decay of $F_S(n)$, which models the decay of Ps in the nanochannels. $F_S(n)$ is heavily dependent on the wall annihilation rate p; as a consequence, the amount of Ps emitted after a prolonged permanence time depends strongly on this parameter, as can be seen in Fig. 10.

Figure 11 shows the dependency of the average energy of the emitted Ps atoms as a function of the permanence time. As the effective mass M dictates the number of interactions required for the thermalization process to take place, it strongly influences such dependency, as can be seen in the figure. Since the rate at which interactions take place scales with the channel size, the channel diameter constitutes the other main contributor to the thermalization time.

TABLE III. Permanence time T_P in the NCP using the isotropic scattering model ($q = 1$) and the corrected model ($q = 3$) calculated for a single dendrite geometry with radius 2 nm $< R <$ 4 nm, a sample temperature of 300 K and an effective mass of 28 u. The permanence time has been calculated as the mean of highest 19% portion of the interaction count distribution. The permanence time almost doubles for higher implantation energies as more deeply implanted Ps requires more interactions to exit the channel.

Implantation energy	$\frac{1}{p}$	T_P ($q = 1$)	T_P ($q = 3$)
7 keV	10^4	0.1 ns	0.2 ns
7 keV	10^5	2 ns	4 ns
7 keV	10^6	4 ns	23 ns
7 keV	∞	5 ns	34 ns
11 keV	10^4	0.2 ns	0.3 ns
11 keV	10^5	4 ns	10 ns
11 keV	10^6	8 ns	42 ns
11 keV	∞	8 ns	56 ns

The permanence time has a well-defined value only in relation to a specific Ps atom being emitted by an NCP and is a distribution of values otherwise. Nonetheless, as the measurement of the exact distribution of permanence times is extremely difficult, literature usually refers to *permanence time* as either the mean or the median permanence time over a specific selection of emitted Ps atoms. Due to the steepness of the distribution (see Fig. 10) different cuts on the selection of Ps onto which the average permanence time is measured can lead to wildly different results.

Measurements of Ps production in pellets of compressed silica powder show thermalization times in the order of 5–25 ns [14,64–66]. From the observation that the energy distribution of Ps emerging from NCPs displays a thermalized component, we expect the permanence time of the thermalized portion of the Ps produced by NCPs to be also in the order of nanoseconds or a few tens of nanoseconds. An indication of the thermalization time of Ps can also be inferred indirectly from the laser delay required in spectroscopy experiments to excite Ps emitted with a velocity close to the thermal one; a recent measurement [40] on NCPs with 10–13 nm diameter channels, held at 300 K and employed with a low implantation energy ($E = 3.5$ keV), places it above 35 ns.

Reference [58] uses a laser to select the positronium emitted by an NCP whose channels have a diameter ranging from 7 to 10 nm a specific time after implantation. It found Ps being emitted 10 ns after implantation to not have yet reached full thermalization, while Ps emitted after 25 ns to be fully thermalized. We can use the tools described in this paper to simulate this experiment, namely, we can use formula (A2) to compute how many interactions will Ps undergo in a certain time and then approximate the energy distribution of Ps by selecting the appropriate $\mathcal{K}_n(E_{Ps})$ spectrum. Figure 12 shows the evolution of the Ps energy spectrum $\mathcal{K}_n(E_{Ps})$ spectrum similarly to Fig. 2, with the difference that the x axis has been labeled with the average interaction time $t_F(n)$ and the parameters of the simulation have been selected to reproduce the NCPs used in [58]. We can see that, in accordance with the

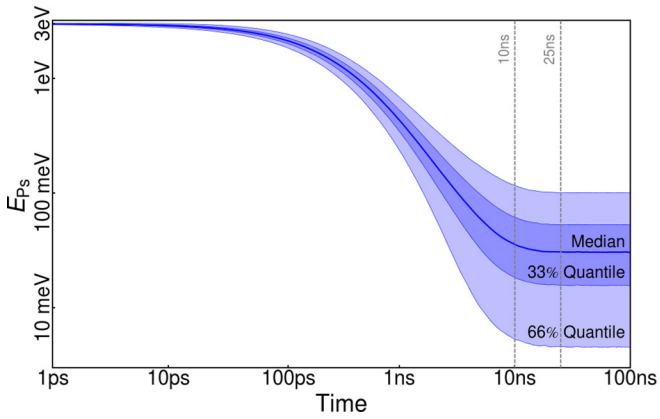

FIG. 12. Evolution of the Ps energy spectra $\mathcal{K}_n(E_{Ps})$ as a function of the average n-interaction time $t_F(n)$. The channel-effective radius has been set to 11.6 nm to reproduce the samples employed in [58] and the effective mass $M = 17.6$ u in accordance with the fit result in the main text (see Table II). We can see how, coherently with [58], thermalization is reached at 25 ns while it is not at 10 ns.

results of [58], thermalization has not been yet reached after 10 ns but it has at the 25 ns mark.

A method to measure directly the Ps permanence time of the thermalized portion has been proposed in [38]; despite a large statistical error, the measurements indicate a thermalization time of the order of 20 ns in NCP with radii of 2.5–4 nm kept at room temperature. To properly compare our results to [38] we need to discriminate, based on the interaction count, which emitted Ps atoms should be classified as warm and which as thermalized or quasithermalized. Measurements performed in NCP (with the same radii of 2.5–4 nm and kept at room temperature) [32] point out that the cold portion of the emitted Ps sums up to around 19%. We will therefore select from the population of Ps that exit the target the 19% fraction that underwent the highest number of interactions before escaping the NCP (expecting it to represent a suitable sample of the cold Ps) and compute its average permanence time. As this method of selecting Ps atoms relies on their likelihood of surviving the NCP to be re-emitted into vacuum, the resulting permanence time will depend on the wall annihilation probability p.

The results are shown in the third and fourth columns of Table III, computed with $q = 1$ and 3, respectively. The cold fraction of Ps [32] being determined to travel in the channel (assuming $p = 10^{-5}$ and an implantation at 7 keV) is around 2 ns. We can see that adopting a value of $q = 1$ results in values of T_P that are generally much lower than the (indicative) experimental values available, regardless of the values of $1/p$. Using, instead, $q = 3$ increases the dependency of the average permanence time on the wall annihilation probability, allowing for a range of values of $1/p$ that yield more realistic values of T_P. For values of $1/p$ of the order of some 10^5, the simulations give a T_P of 4–23 ns (for $E = 7$ keV) and 10–42 ns (for $E = 11$ keV) that are consistent with the experimental indications of Refs. [32,38]. Note that in these computations the NCP temperature and effective mass have only minor influence on the permanence time (the latter due to the fact that we are selecting the colder Ps by fraction and not by absolute value of its energy).

APPENDIX B: QUALITATIVE EXPLANATION OF THE TWO-POPULATION ENERGY SPECTRUM

As mentioned in the Introduction, the energy spectrum of the Ps produced by means of NCP converters has been measured in previous experiments and has been empirically characterized as the sum of two thermal distributions [32,38]; this feature, however, had so far no explanation. More precisely, a fraction (around 10% to 30%) of the emitted Ps thermalizes to a low temperature, which approximately corresponds to the temperature of the NCP, while it seems that the remaining fraction of Ps is thermally distributed at a much higher temperature. This observation could have led to hypothesize the existence of two distinct underlying physical phenomena, one of which generates low-temperature Ps and the other responsible for the production of high-temperature Ps. One of the most striking insights arising from our simulations is that, instead, a single continuous process, the scattering and cooling of Ps within the nanochannels, is able to reproduce the supposedly two-temperature feature of the experimentally observed Ps energy spectrum.

We perform an empirical analysis by classifying the emitted positronium into three families, depending on the number of wall interactions it underwent before leaving the channel. The ansatz is that Ps atoms that have bounced off the channel walls several times lose most of their energy and thus approach a thermal distribution at the NCP temperature, thus generating the cold Ps fraction. The family of Ps having undergone an intermediate number of interactions escapes the NCP on average at a higher energy, and presents a spectrum resembling a high-temperature distribution. Finally, Ps that undergoes too few interactions leaves the sample with a very high speed, such that they would not be detectable with typical ToF measurements. The cuts between the three families have been chosen artfully so as to render our explanation as clear and evident as possible.

We consider a simulation in which we implant 7 keV positrons in a NCP with channel radius $R = 4$ nm at a temperature of 300 K. We scatter the Ps inside the NCP channels with an effective mass $M = 16$ u with an angular distribution generated with $q = 3$ and a wall annihilation factor of $1/p = 10^5$. These parameters have been chosen to generate the plots in Fig. 13; nonetheless, we have verified through numerical simulations that the considerations presented in this section are valid for a wide range of simulation parameters.

While dividing the Ps in three families according to the number of interactions, we do not use sharp cuts but, instead, we employ two smooth transition zones; in each zone, each Ps is assigned to a family or to the adjacent family with a probability which depends on the number of interactions with the walls, as shown in Fig. 13(a). Figure 13(b) then shows how the interaction count spectrum $\mathcal{S}(n)$ gets divided among the three families when applying the partitioning presented in Fig. 13(a). Since we consider Ps escaping the channels instead of the Ps being produced, the three distributions do not sum up to $\mathcal{S}(n)$: the missing portion is the Ps that annihilates before escaping to the vacuum. This fraction [hatched gray area in

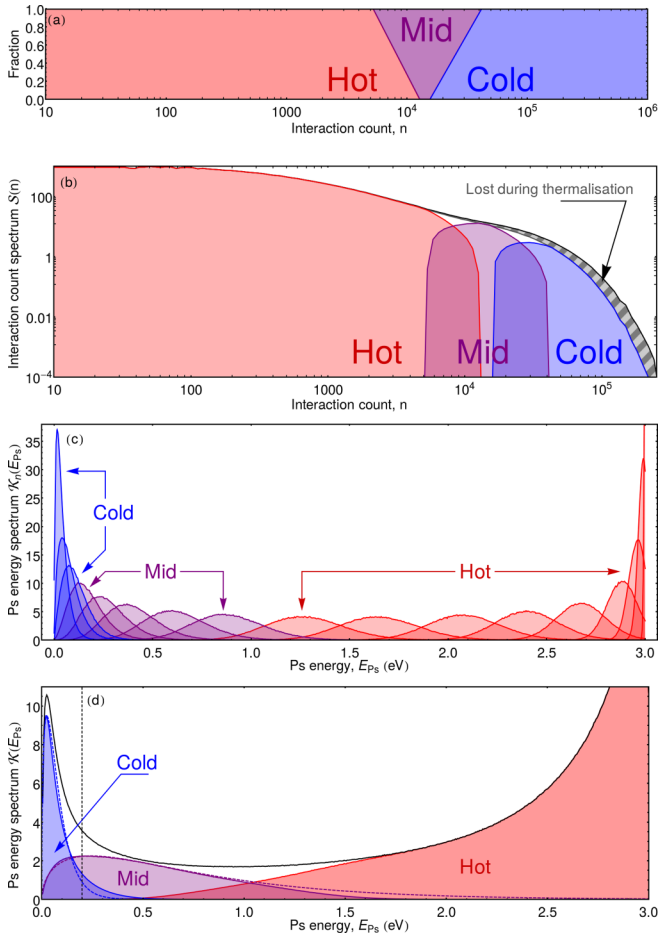

FIG. 13. The mechanism that leads to the Ps spectrum exhibiting two thermal distributions, illustrated following the detailed description of the process given in Appendix B. (a) Subdivision of the generated Ps population into three families, based on the number of interactions with the walls required to exit the NCP. (b) Resulting division of the *interaction count spectrum* (with Ps loss due to annihilation in the NCP as the hatched gray area). (c) Evolution of the energy distribution of Ps atoms in an NCP as a function of the number of wall interactions (the color indicates the transition between different families). (d) The final energy spectrum at which each of the three families is emitted; note the coldest two mimic a thermal distribution in the lower portion of the 0–3 eV range.

the plot of Fig. 13(b)] corresponds to the term $1 - F_S(n)$ in Eq. (6).

Figure 13(c) shows the evolution of the energy distribution of Ps atoms as the number of interactions they underwent increases; the transitions between the three families are marked with corresponding colors. As the cooling progresses, the production distribution (δ distribution located at 3 eV) spreads out, turning in a larger distribution resembling (as consequence of the central limit theorem) the normal distribution. This distribution then travels toward the thermal distribution and, as it approaches zero, it compresses again. Thus, while approaching the equilibrium thermal distribution, the distribution loses its symmetry and then settles into its final shape. We marked and colored the successive phases of the cooling process according to the distribution (*hot*, *mid*, or *cold*) to which we assigned most of the Ps atoms that have reached such cooling step when they left the NCP.

Finally, Fig. 13(d) illustrates how the three families contribute to the final shape of the Ps spectrum. The *cold* family consists mainly of Ps atoms that have completely reached thermalization and, therefore, closely resembles a thermal distribution at a temperature only moderately higher than that of the NCP sample, and the temperature difference stems from the contribution of incompletely thermalized, higher-energy distributions. The *hot* family sums to a heavy tail located entirely at very high energies, corresponding to particles that are too fast to be detected by ToF measurements [the dashed vertical line in Fig. 13(d) marks 0.2 eV, which is a fair indication of the region our reference ToF experiments are sensitive in [32,38,45]]. Finally, the *mid* family consists of Ps having an intermediate energy, close to the upper end of energies that are accessible in typical ToF measurements. From Fig. 13(c), we can see that the cooling process slows down when approaching zero and, at the same time, the distributions become more compressed at low energies. As a consequence, the shape of the *mid* portion is heavier at lower energies and, therefore, mimics a thermal distribution. Since in the 0–0.5 eV region the *hot* portion contributes negligibly, the data analysis in this energy range will result in the observation of a spectrum that seems to be composed of two thermal distributions. The best fit to the energy spectrum simulated in this example is given by a *cold* (dashed blue) fraction and *mid* (dashed purple) fraction having temperatures of 600 and 6600 K, respectively. The relatively high temperature of the *cold* fraction is due to the large channels and high value of M we have chosen for this specific simulation: thinner channels and lower effective masses yield temperatures closer to the sample temperature.

In summary, we can conclude that the low-temperature fraction of the energy spectrum indeed corresponds to particles that are (almost) fully thermalized, while the high-energy component is the sum of several nonthermal distributions whose shape resembles a thermal distribution, for kinetic energies below 0.5 eV. At higher energies, the deviation from a thermal distribution becomes rapidly very stark, but these energies are not accessible with typical ToF measurements, hence the appearance of two thermal distributions.

[1] D. W. Gidley, H. G. Peng, and R. S. Vallery, Positron annihilation as a method to characterize porous materials, Annu. Rev. Mater. Res. **36**, 49 (2006).

[2] C. He, T. Oka, Y. Kobayashi, N. Oshima, T. Ohdaira, A. Kinomura, and R. Suzuki, Positronium annihilation and pore surface chemistry in mesoporous silica films, Appl. Phys. Lett. **91**, 024102 (2007).

[3] C. Hugenschmidt and H. Ceeh, The free volume in dried and H_2O-loaded biopolymers studied by positron lifetime measurements, J. Phys. Chem. B **118**, 9356 (2014).

[4] M. P. Petkov, M. H. Weber, K. G. Lynn, and K. P. Rodbell, Porosity characterization by beam-based three-photon positron annihilation spectroscopy, Appl. Phys. Lett. **77**, 2470 (2000).

[5] R. S. Brusa, M. Spagolla, G. P. Karwasz, and A. Zecca, Porosity in low dielectric constant SiOCH films depth profiled by positron annihilation spectroscopy, J. Appl. Phys. **95**, 2348 (2004).

[6] R. S. Brusa, C. Macchi, S. Mariazzi, and G. P. Karwasz, Porosity of low-κ materials studied by slow positron beam, Acta Phys. Pol. A **107**, 702 (2005).

[7] R. Checchetto, N. Patel, A. Miotello, and R. S. Brusa, Nanolayers on nanochannels for hydrogen purification, J. Appl. Phys. **105**, 034502 (2009).

[8] M. Gomaa, C. Hugenschmidt, M. Dickmann, E. E. Abdel-Hady, H. F. M. Mohamed, and M. O. Abdel-Hamed, Crosslinked PVA/SSA proton exchange membranes: correlation between physiochemical properties and free volume determined by positron annihilation spectroscopy, Phys. Chem. Chem. Phys. **20**, 28287 (2018).

[9] W. F. Yong, F. Y. Li, Y. C. Xiao, T. S. Chung, and Y. W. Tong, High performance PIM-1/Matrimid hollow fiber membranes for CO_2/CH_4, O_2/N_2 and CO_2/N_2 separation, J. Membr. Sci. **443**, 156 (2013).

[10] D. Roilo, C. A. Maestri, M. Scarpa, P. Bettotti, W. Egger, T. Koschine, R. S. Brusa, and R. Checchetto, Cellulose nanofibrils films: Molecular diffusion through elongated sub-nano cavities, J. Phys. Chem. C **121**, 15437 (2017).

[11] A. Naderi, A. A. Tashvigh, and T.-S. Chung, H_2/CO_2 separation enhancement via chemical modification of polybenzimidazole nanostructure, J. Membr. Sci. **572**, 343 (2019)

[12] Y. Li, R. Zhang, H. Chen, J. Zhang, R. Suzuki, T. Ohdaira, M. M. Feldstein, and Y. C. Jean, Depth profile of free volume in a mixture and copolymers of poly(N-vinyl-pyrrolidone) and poly(ethylene glycol) studied by positron annihilation spectroscopy, Biomacromolecules **4**, 1856 (2003).

[13] D. B. Cassidy, Experimental progress in positronium laser physics, Eur. Phys. J. D **72**, 53 (2018).

[14] D. B. Cassidy, P. Crivelli, T. H. Hisakado, L. Liszkay, V. E. Meligne, P. Perez, H. W. K. Tom, and A. P. Mills Jr., Positronium cooling in porous silica measured via Doppler spectroscopy, Phys. Rev. A **81**, 012715 (2010).

[15] L. Gurung, T. J. Babij, S. D. Hogan, and D. B. Cassidy, Precision Microwave Spectroscopy of the Positronium $n = 2$ Fine Structure, Phys. Rev. Lett. **125**, 073002 (2020).

[16] S. Aghion, C. Amsler, A. Ariga, T. Ariga, G. Bonomi, P. Bräunig, J. Bremer, R. S. Brusa, L. Cabaret, M. Caccia *et al.* (AEgIS Collaboration), Laser excitation of the n=3 level of positronium for antihydrogen production, Phys. Rev. A **94**, 012507 (2016).

[17] S. Aghion, C. Amsler, M. Antonello, A. Belov, G. Bonomi, R. S. Brusa, M. Caccia, A. Camper, R. Caravita, F. Castelli *et al.* (AEgIS Collaboration), Producing long-lived 23S positronium via 33P laser excitation in magnetic and electric fields, Phys. Rev. A **98**, 013402 (2018).

[18] D. B. Cassidy, T. H. Hisakado, H. W. K. Tom, and A. P. Mills Jr., Efficient Production of Rydberg Positronium, Phys. Rev. Lett. **108**, 043401 (2012).

[19] D. B. Cassidy, T. H. Hisakado, H. W. K. Tom, and A. P. Mills Jr., Optical Spectroscopy of Molecular Positronium, Phys. Rev. Lett. **108**, 133402 (2012).

[20] D. B. Cassidy, T. H. Hisakado, H. W. K. Tom, and A. P. Mills, Positronium Hyperfine Interval Measured via Saturated Absorption Spectroscopy, Phys. Rev. Lett. **109**, 073401 (2012)

[21] A. Kellerbauer, M. Amoretti, A. S. Belov, G. Bonomi, I. Boscolo, R. S. Brusa, M. Büchner, V. M. Byakov, L. Cabaret, C. Canali *et al.* (AEgIS Proto-Collaboration), Proposed antimatter gravity measurement with an antihydrogen beam, Nucl. Instrum. Methods Phys. Res., Sect. B **266**, 351 (2008).

[22] P. Crivelli, D. A. Coole, and S. Friederich, Experimental considerations for testing antimatter antigravity using positronium 1S-2S spectroscopy, Int. J. Mod. Phys. Conf. Ser. **30**, 1460257 (2014).

[23] D. B. Cassidy and S. D. Hogan, Atom control and gravity measurements using Rydberg positronium, Int. J. Mod. Phys. Conf. Ser. **30**, 1460259 (2014).

[24] M. K. Oberthaler, Anti-matter wave interferometry with positronium, Nucl. Instrum. Methods Phys. Res., Sect. B **192**, 129 (2002).

[25] P. M. Platzman and A. P. Mills Jr., Possibilities for Bose condensation of positronium, Phys. Rev. B **49**, 454 (1994).

[26] H. Iijima, T. Asonuma, T. Hirose, M. Irako, T. Kumita, M. Kajita, K. Matsuzawa, and K. Wada, Laser cooling system of ortho-positronium, Nucl. Instrum. Methods Phys. Res., Sect. A **455**, 104 (2000).

[27] P. Perez and A. Rosowsky, A new path toward gravity experiments with antihydrogen, Nucl. Instrum. Methods Phys. Res., Sect. A **545**, 20 (2005).

[28] M. Doser, C. Amsler, A. Belov, G. Bonomi, P. Bräunig, J. Bremer, R. Brusa, G. Burkhart, L. Cabaret, C. Canali *et al.* (AEgIS Collaboration), Exploring the WEP with a pulsed cold beam of antihydrogen, Class. Quantum Grav. **29**, 184009 (2012).

[29] L. Liszkay, F. Guillemot, C. Corbel, J.-P. Boilot, T. Gacoin, E. Barthel, P. Pérez, M.-F. Barthe, P. Desgardin, P. Crivelli, U. Gendotti, and A. Rubbia, Positron annihilation in latex-templated macroporous silica films: Pore size and ortho-positronium escape, New J. Phys. **14**, 065009 (2012).

[30] S. Mariazzi, L. Toniutti, N. Patel, and R. S. Brusa, Formation and escaping of positronium in porous SiO 2 films at low temperature, Appl. Surf. Sci. **255**, 191 (2008).

[31] S. Mariazzi, P. Bettotti, S. Larcheri, L. Toniutti, and R. S. Brusa, High positronium yield and emission into the vacuum from oxidized tunable nanochannels in silicon, Phys. Rev. B **81**, 235418 (2010).

[32] S. Mariazzi, P. Bettotti, and R. S. Brusa, Positronium Cooling and Emission in Vacuum from Nanochannels at Cryogenic Temperature, Phys. Rev. Lett. **104**, 243401 (2010).

[33] S. Mariazzi, B. Rienäcker, R. Magrin Maffei, L. Povolo, S. Sharma, R. Caravita, L. Penasa, P. Bettotti, M. Doser, and R. S. Brusa, Phys. Rev. B **105**, 115422 (2022).

[34] B. S. Cooper, A. M. Alonso, A. Deller, L. Liszkay, and D. B. Cassidy, Phys. Rev. B **93**, 125305 (2016).

[35] F. Guatieri, S. Mariazzi, and R. S. Brusa, Monte Carlo simulation of the implantation profile of e+ in nanochanneled silicon, Eur. Phys. J. D **72**, 198 (2018).

[36] Y. Nagashima, Y. Morinaka, T. Kurihara, Y. Nagai, T. Hyodo, T. Shidara, and K. Nakahara, Origins of positronium emitted from SiO_2, Phys. Rev. B **58**, 12676 (1998).

[37] R. S. Brusa and A. Dupasquier, Positronium emission and cooling, in *Proceedings of the International School of Physics "Enrico Fermi"* (IOS Press, Amsterdam, 2009).

[38] S. Mariazzi, L. Di Noto, G. Nebbia, and R. S. Brusa, Collisional cooled Ps emitted into vacuum from silica-based porous materials: Experiment to measure the Ps cooling time, J. Phys.: Conf. Ser. **618**, 012039 (2015).

[39] R. Caravita, Towards measuring gravity on neutral antimatter. Ph.D. Thesis, Università degli studi di Genova, 2017.

[40] C. Amsler, M. Antonello, A. Belov, G. Bonomi, R. S. Brusa, M. Caccia, A. Camper, R. Caravita, F. Castelli, G. Cerchiari *et al.* (AEgIS Collaboration), Velocity-selected production of 23S metastable positronium, Phys. Rev. A **99**, 033405 (2019).

[41] S. Mariazzi, A. Salemi, and R. S. Brusa, Positronium cooling into nanopores and nanochannels by phonon scattering, Phys. Rev. B **78**, 085428 (2008).

[42] P. Crivelli, U. Gendotti, A. Rubbia, L. Liszkay, P. Perez, and C. Corbel, Measurement of the orthopositronium confinement energy in mesoporous thin films, Phys. Rev. A **81**, 052703 (2010).

[43] K. Shu, A. Ishida, T. Namba, S. Asai, N. Oshima, B. E. O'Rourke, and K. Ito, Observation of orthopositronium thermalization in silica aerogel at cryogenic temperatures, Phys. Rev. A **104**, L050801 (2021).

[44] M. Antonello, A. Belov, G. Bonomi, R. S. Brusa, M. Caccia, A. Camper, R. Caravita, F. Castelli, D. Comparat, G. Consolati *et al.* (AEgIS Collaboration), Rydberg-positronium velocity and self-ionization studies in a 1T magnetic field and cryogenic environment, Phys. Rev. A **102**, 013101 (2020).

[45] F. Guatieri, S. Mariazzi, L. Penasa, G. Nebbia, C. Hugenschmidt, and R. S. Brusa, Time-of-flight apparatus for the measurement of slow positronium emitted by nanochannel converters at cryogenic temperatures, Nucl. Instrum. Methods Phys. Res., Sect. B **499**, 32 (2021).

[46] F. Guatieri, S. Mariazzi, and R. S. Brusa, Simulating positron to positronium conversion in nanostructured materials, Acta Phys. Pol. A **137**, 113 (2020).

[47] R. Paulin and G. Ambrosino, *Anomalous Long Annihilation Lean Lives of Positrons, Proceedings of the Conference held at Wayne State University July 27-29, 1965* (Academic, New York, 1967).

[48] W. C. Sauder, Thermalization by elastic collisions: Positronium in a rare gas moderator, J. Res. Natl. Bur. Stand. **72A**, 91 (1968).

[49] M. Kakimoto, Y. Nagashima, T. Hyodo, K. Fujiwara, and T. B. Chang, Slowing-down of positronium in gases, in *Positron Annihilation*, edited by L. Dorikens-Vanpraet, M. Dorikens, and D. Segers (World-Scientific, Singapore, 1989), p. 737; T. Hyodo, M. Kaimoto, T. B. Chang, J. Deng, T. Akahane, T. Chiba, B. T. A. McKee, and A. T. Stewart, Relaxation of the momentum distribution of free positronium atoms interacting with silica fine particles, in *Positron Annihilation*, edited by L. Dorikens-Vanpraet, M. Dorikens, and D. Segers (World-Scientific, Singapore, 1989), p. 878.

[50] Y. Nagashima, M. Kakimoto, T. Hyodo, K. Fujiwara, A. Ichimura, T. Chang, J. Deng, T. Akahane, T. Chiba, K. Suzuki, B. T. McKee, and A. T. Stewart, Thermalization of free positronium atoms by collisions with silica-powder grains, aerogel grains, and gas molecules, Phys. Rev. A **52**, 258 (1995).

[51] M. Skalsey, J. J. Engbrecht, R. K. Bithell, R. S. Vallery, and D. W. Gidley, Thermalization of Positronium in Gases, Phys. Rev. Lett. **80**, 3727 (1998).

[52] M. Skalsey, J. J. Engbrecht, C. M. Nakamura, R. S. Vallery, and D. W. Gidley, Doppler-broadening measurements of positronium thermalization in gases, Phys. Rev. A **67**, 022504 (2003).

[53] L. D. Landau and E. M. Lifschitz, *Course of Theoretical Physics*, Volume I, Mechanics (Pergamon, New York, 1960).

[54] H. Saito and T. Hyodo, *New Directions in Antimatter Chemistry and Physics* (Kluwer Academic, Dordrecht, 2001), Chap. 7.

[55] F. Guatieri, Production and excitation of cold Ps for $\bar{H}$ formation by charge exchange: Towards a gravitational measurement on antimatter. Ph.D. Thesis, Università degli studi di Trento, 2018.

[56] B. S. Cooper, J.-P. Boilot, C. Corbel, F. Guillemot, L. Gurung, L. Liszkay, and D. B. Cassidy, Annihilation of positronium atoms confined in mesoporous and macroporous SiO_2 films, Phys. Rev. B **97**, 205302 (2018).

[57] S. Mariazzi, L. DiNoto, L. Ravelli, W. Egger, and R. S. Brusa, Study of Positronium formation in nano-channelled silicon as a function of sample temperature, J. Phys.: Conf. Ser. **443**, 012061 (2013).

[58] S. Mariazzi, R. Caravita, C. Zimmer, B. Rienäcker, A. Camper, A. Belov, G. Bonomi, R. S. Brusa, F. Castelli, G. Consolati *et al.* (AEgIS Collaboration), High-yield thermalized positronium at room temperature emitted by morphologically tuned nanochanneled silicon targets, J. Phys. B: At., Mol. Opt. Phys. **54**, 085004 (2021).

[59] A. P. Mills Jr., Positronium Formation at Surfaces, Phys. Rev. Lett. **41**, 1828 (1978).

[60] B. Rienäcker, T. Gigl, G. Nebbia, F. Pino, and C. Hugenschmidt, Absolute fraction of emitted Ps determined by GEANT4-supported analysis of gamma spectra, Phys. Rev. A **102**, 062212 (2020).

[61] S. Aghion, C. Amsler, A. Ariga, T. Ariga, A. S. Belov, G. Bonomi, P. Bräunig, J. Bremer, R.S. Brusa, L. Cabaret *et al.* (AEgIS Collaboration), Positron bunching and electrostatic transport system for the production and emission of dense positronium clouds into vacuum, Nucl. Instrum. Methods Phys. Res., Sect. B **362**, 86 (2015).

[62] B. T. Phong, Illumination for computer generated pictures, Commun. ACM **18**, 311 (1975).

[63] L. Di Noto, S. Mariazzi, M. Bettonte, G. Nebbia, and R. S. Brusa, Time of Flight system to investigate positronium cooling, Eur. Phys. J. D **66**, 118 (2012).

[64] S. Takada, T. Iwata, K. Kawashima, H. Saito, Y. Nagashima, and T. Hyodo, Thermalization of positronium atoms studied with time-resolved angular correlation of annihilation radiation, Radiat. Phys. Chem. **58**, 781 (2000).

[65] C. Dauwe, B. Van Waeyenberge, D. Segers, T. Van Hoecke, and J. Kuriplach, Some aspects of the interactions of orthopositronium with perfect and defect surfaces of insulating materials, J. Radiol. Nucl. Chem. **210**, 293 (1996).

[66] A. Deller, B. S. Cooper, T. E. Wall, and D. B. Cassidy, Positronium emission from mesoporous silica studied by laser-enhanced time-of-flight spectroscopy, New J. Phys. **17**, 043059 (2015).